Numerical investigation of three-dimensional asymmetric hovering flapping flight

D. Diaz-Arriba[1], T. Jardin[1], N. Gourdain[1], F. Pons[2], L. David[2][1]

[1]*ISAE-SUPAERO, Université de Toulouse, Toulouse, France*

[2]*Institut Pprime, UPR 3346, CNRS-Université de Poitiers-ENSMA, Poitiers, France*

Direct numerical simulations are performed to assess the aerodynamic performance of three-dimensional wings undergoing asymmetric hovering flapping flight. A large number of flapping kinematics is investigated, varying the pitch rate and the upstroke and downstroke angles of attack. We show that, for all cases, time-average performance is driven, to leading order, by the mean angle of attack over a flapping period despite the increased contribution of drag to vertical force with increased stroke plane angle. We hence suggest that asymmetric hovering is not intrinsically more efficient than normal hovering, conversely to what has been previously reported in the literature. This may explain the underrepresentation of this flight mode in nature.

I. INTRODUCTION

Most insects achieve hovering flight by flapping their wings along a nearly horizontal plane[1], a flight mode commonly referred to as 'normal hovering'. However, some of the best hoverers flap their wings along an inclined stroke plane. Typical examples include dragonflies and true hoverflies. Yet, because of this overrepresentation of species employing 'normal hovering' in nature, this flight mode has attracted much more attention than its 'non-normal hovering' counterpart.

In 'normal hovering', the drag is directed along the horizontal wing path. The hovering condition implies that its time-average over a flapping cycle is zero. In other words, the drag experienced by the wing during downstroke balances that experienced during upstroke. In that case, the lift is perpendicular to the horizontal wing path and is hence the only contributor to the vertical force required to balance the insect weight.

In 'non-normal hovering', the wing flaps along an inclined stroke plane and the drag is not directed horizontally. The latter contributes, with the lift, to both vertical and horizontal forces and the inclination of the stroke plane is determined by ensuring that the time-average horizontal force is zero over a flapping cycle, which in terms of lift and drag writes $\beta = \arctan(\bar{D}/\bar{L})$, where β, $\bar{L}$ and $\bar{D}$ are the stroke plane angle and time-averaged lift and drag forces, respectively. This implies that the drag experienced during downstroke does not balance that experienced during upstroke, which occurs in particular when the downstroke kinematics is not a mirror image of the upstroke, for symmetric airfoils. Accordingly, this 'non-normal hovering' mode is sometimes referred to as 'asymmetric hovering'. We note that a clear distinction should be made between hovering and forward flight. The latter commonly relies on wings flapping along an inclined stroke plane (i.e. the plane angle is known to increase with flight speed[2,3]) and has thus been extensively studied in the literature (see recent works by[4,5], for example). It is also worth mentioning that in forward flight, asymmetric kinematics of symmetric airfoils do not necessarily imply that the stroke plane is inclined. The present paper focuses exclusively on hovering flight.

The contribution of drag to the vertical force in hovering flight has been nicely highlighted by[6] using two-dimensional numerical simulations. In particular, the comparison between two idealized 'normal' and 'non-normal' hovering modes first revealed that the vertical-to-horizontal force ratio was 0.66 and 1.31, respectively, with the drag contributing to 76% of

the vertical force in the latter case. It was thus suggested that 'non-normal hovering' could be more efficient than 'normal hovering', which questions previous hypothesis by[1]. More generally,[6] systematically varied the stroke plane angle from 0° to 90° and demonstrated that while the vertical force remains roughly constant from 0° to 60° and then decreases, the horizontal force continuously decreases from 0° to 90° leading to a continuous increase in the vertical-to-horizontal force ratio. In conclusion,[6] further suggested that aerodynamic efficiency could be further improved by removing the upstroke, assuming that an upstroke with zero angle of attack contributes almost no force.

Wings flapping along an inclined stroke plane were further investigated by[7] using two-dimensional numerical simulations. Specifically, the Reynolds number, the stroke amplitude and the rotational timing and duration were systematically varied to assess their influence on aerodynamic performance. Asymmetry was imposed by prescribing different upstroke and downstroke angles of attack.[7] corroborated results of[6] in that drag can account for most of the vertical force produced during one flapping cycle. They showed that a peculiar feature of asymmetric hovering was the absence of significant wake capture mechanism during downstroke, due to the relatively weak upstroke angle of attack and the absence of significant leading edge vortices (LEV). This was in line with previous experimental results of[8] obtained using time-resolved particle image velocimetry (PIV) and non-intrusive load measurements. In this study, the authors reported that, in some cases, the absence of significant wake capture promote a smoother development of the LEV close to the airfoil surface, which may partly be responsible for an enhancement in lift with asymmetry (i.e. with stroke plane angle). Moreover, enhancement in vertical-to-drag force ratio (i.e. efficiency) with asymmetry was here again put into evidence, although reservations were expressed on the evaluation of drag through momentum approaches. More recently,[9] numerically investigated the aerodynamic performance of 'non-normal hovering', where asymmetry was introduced by prescribing different upstroke and downstroke angles of attack and/or different upstroke and downstroke durations. Their results, which were obtained in a two-dimensional framework, supported previous studies in that both lift and efficiency could be enhanced by asymmetry.

Overall, past studies suggested that asymmetric kinematics could lead to enhanced aerodynamic performance of hovering flapping wings. However, only few studies addressed this opportunity and virtually all considered two-dimensional configurations despite prominent three-dimensional effects in such revolving wing configurations[10–12]. A notable exception

is the work by[13] who experimentally investigated the role of asymmetric strokes on aerodynamic performance by prescribing different upstroke and downstroke angles of attack, highlighting an increase in vertical force with asymmetry. We note that a few additional studies focus on one specific case, usually representative of a given species, and do not systematically vary kinematic parameters[14,15]. On the other hand, while enhancement in aerodynamic performance with asymmetry has been correlated with peculiar flow phenomena (e.g. wake capture), it remains unclear what specific parameter drives this trend. This is related to the fact that the introduction of asymmetry in a reference, symmetrical flapping motion implies variations in more than one parameter (e.g. angles of attack and rotational speed), and may hence affect different mechanism, including wake capture, Kramer and added mass effects. Therefore, the goal of the present study is to understand the role of kinematic parameters on aerodynamic performance of asymmetric hovering flapping flight by covering a relatively large parameter space, in a three-dimensional framework.

To this aim, we directly solve the three-dimensional Navier-Stokes equations to predict the aerodynamic performance of asymmetric hovering flapping motions. Asymmetry is imposed by setting different upstroke and downstroke angles of attack. We first conduct numerical simulations with relatively low temporal and spatial resolutions to explore a significant portion of the parameter space and subsequently put into evidence prominent trends in aerodynamic performance with parameter variations. We then focus on optimal lift and/or efficiency cases for which we analyze the unsteady aerodynamics using numerical simulations with higher temporal and spatial resolutions. Finally, we extend our results to kinematics with different pitch rates. All these results indicate that asymmetric hovering is not intrinsically more efficient than normal hovering, conversely to what has been previously reported in the literature, which may explain the underrepresentation of this flight mode in nature.

II.   NUMERICAL METHODS

We consider a three-dimensional wing undergoing the flapping kinematics shown in figure 1. The kinematics consists of combined revolving and pitching motions, with angular speeds $\dot{\phi}$ and $\dot{\alpha}$ respectively. The revolving amplitude is set to $\phi_0 = 120°$. The time histories of $\dot{\phi}$ and $\dot{\alpha}$ along a flapping period T are displayed in figure 1 for a reference, symmetric case where the angles of attack of the stroke and returning stroke are set to $\alpha_1 = 45°$
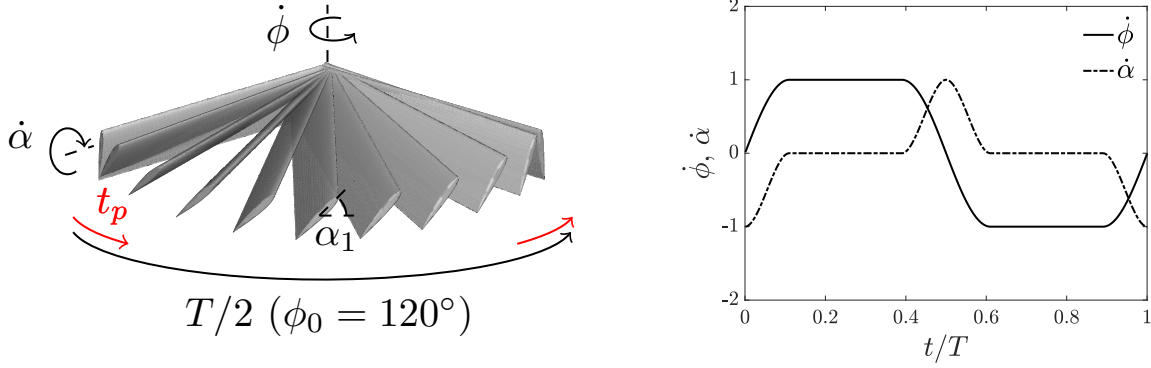
FIG. 1. Kinematics of the flapping wing (left, one stroke) and corresponding time evolution of revolving and pitching speeds (right, two strokes) for a reference symmetric case.

and $\alpha_2 = 45°$, respectively. Note that angles of attack are defined with respect to the direction of the revolving motion, with α_1 and α_2 denoting the angle of attack when the motion is from left to right and from right to left (see figure 1), respectively. $\dot{\phi}$ and $\dot{\alpha}$ are constant over $T/2 - t_p$ and vary at the end and at the beginning of each stroke, over t_p. Varying velocity profiles are described using 3rd and 4th order polynomials, for pitching and revolving motions respectively, that ensure continuity in wing acceleration. Accordingly, the instantaneous values for α and ϕ read:

$$\alpha = a_\alpha + b_\alpha t + c_\alpha t^2 + d_\alpha t^3 + e_\alpha t^4 \tag{1}$$

with constants a_α, b_α, c_α, d_α, e_α determined from constraints on α, $\dot{\alpha}$ and $\ddot{\alpha}$. For example, the first pronation phase is characterized by $\ddot{\alpha}(0) = 0$, $\ddot{\alpha}(t_p) = 0$, $\dot{\alpha}(t_p) = 0$, $\alpha(0) = \alpha_i$ and $\alpha(t_p) = \alpha_1$, where α_i is the angle of attack at the beginning of the stroke (90° in symmetric cases, as shown in figure 1).

$$\phi = a_\phi + b_\phi t + c_\phi t^2 + d_\phi t^3 + e_\phi t^4 + f_\phi t^5 \tag{2}$$

with constants a_ϕ, b_ϕ, c_ϕ, d_ϕ, e_ϕ, f_ϕ determined from constraints on ϕ, $\dot{\phi}$, $\ddot{\phi}$ and $\dddot{\phi}$. The first pronation phase is characterized by $\phi(0) = \phi_i$, $\phi(t_p) = \phi_{t_p}$, $\dot{\phi}(0) = 0$, $\dot{\phi}(t_p) = U/(0.716R)$ and $\dddot{\phi}(0) = 0$, where ϕ_i is the wing position at the beginning of the stroke (arbitrary) and $\phi_{t_p} = \phi_i + (\phi_0/2) - Ut_p/(0.716R)$ is the wing position at t_p.

The Reynolds number based on the wing chord c and the velocity U at the $r = 0.716R$
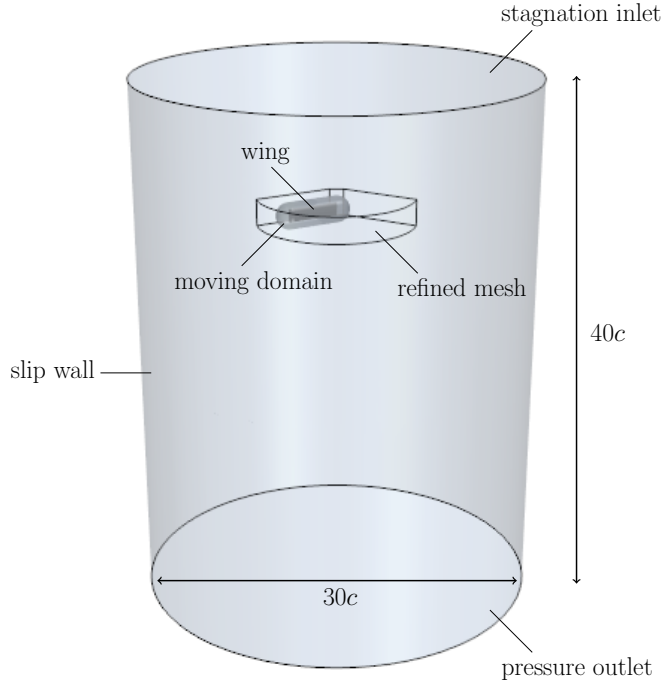
5

FIG. 2. Sketch of the computational domain.

radial position during the constant revolving speed phase is set to 1000, where R is the radius of the wing (at this radial position the 120° revolving amplitude corresponds to 6 chords of travel, as initially used in the 2D experiments of[8]). The wing is a NACA0012 profile extruded in the radial direction with constant chord c and without twist. The aspect ratio is equal to $R/c = 4$ (the wing revolves about its root, i.e. there is no root cutout, hence the radius is equal to the span) which was previously found to be the optimal lift aspect ratio for revolving wings at similar Reynolds numbers[16]. In what follows, α_1 and α_2 are systematically varied to assess the influence of asymmetry on aerodynamic performance. Recall that $\alpha_1 = \alpha_2$ corresponds to symmetric motions while $\alpha_1 \neq \alpha_2$ corresponds to asymmetric motions.

The flow around the flapping wing is computed using the flow solver StarCCM+. The latter directly solves the three-dimensional Navier-Stokes equations using a cell-centered finite volume method. An overset mesh approach is employed where the wing is embedded in a small cylindrical domain which moves in a larger background cylindrical domain, as shown in figure 2 (also see appendix A). The wing is modelled as a non-slip wall and flaps along a path that is parallel to the top and bottom boundaries of the background cylindrical domain. The latter are treated as stagnation inlet and pressure outlet (farfield reference

6

pressure), respectively, while lateral boundaries are treated as slip walls. Momentum and continuity equations are solved in an uncoupled way using a predictor-corrector approach. Specifically, a colocated variable arrangement and a Rhie–Chow-type pressure–velocity coupling combined with a SIMPLE-type algorithm are used. Second order numerical schemes are employed for both spatial and temporal discretizations. The numerical method is further detailed in the works by[17] and[18]. It has been previously validated over a relatively large spectrum of low Reynolds number applications including axisymmetric bluff bodies[19], revolving wings[20] and perching airfoils[21].

Numerical simulations are first performed for the reference, symmetric case $\alpha_1 = \alpha_2 = 45°$ with different spatial and temporal resolutions. Three spatial resolutions are considered with typical cell dimensions on the wing surface equal to $\Delta x_s = 0.02c$, $0.01c$ and $0.005c$ and typical dimensions in the vicinity of the wing (i.e. within the small, moving cylindrical domain) equal to $\Delta x_v = 0.04c$, $0.02c$ and $0.01c$. Similarly, three temporal resolutions are considered with time steps equal to $\Delta t = T/250$, $T/500$ and $T/1000$. Figure 3 shows the lift coefficients period-averaged over each of the first ten flapping periods for the different spatial and temporal resolutions. Dashed lines depicts the $\pm 2.5\%$ bounds around the value obtained for $\Delta x_s = 0.005c$ and $\Delta t = T/1000$ at the tenth period. It can be observed that all cases approximate this value within $\pm 2.5\%$, as early as the second period. That is, the results are independent to both spatial and temporal resolutions, within $\pm 2.5\%$, and strong initial transients are found to rapidly decay, within one flapping period.

III. RESULTS

A. Overall analysis

Low resolution cases with $\Delta x_s = 0.02c$ and $\Delta t = T/250$ are first used to systematically analyze the aerodynamic performance of cases with angles of attack in the range $[0° - 90°]$. Figure 4 shows the mean vertical force coefficient $\bar{C}_V$ as a function of the mean vertical force coefficient to power coefficient ratio, $\bar{C}_V / \bar{C}_P$.

Mean values are here obtained by averaging instantaneous values over the third flapping period. C_V results from the contribution of both lift L and drag D through the stroke plane angle β: $C_V = 2(L\cos\beta + D\sin\beta)/\rho S U^2$ where $\beta = \arctan \bar{D}/\bar{L}$ and U is the velocity at
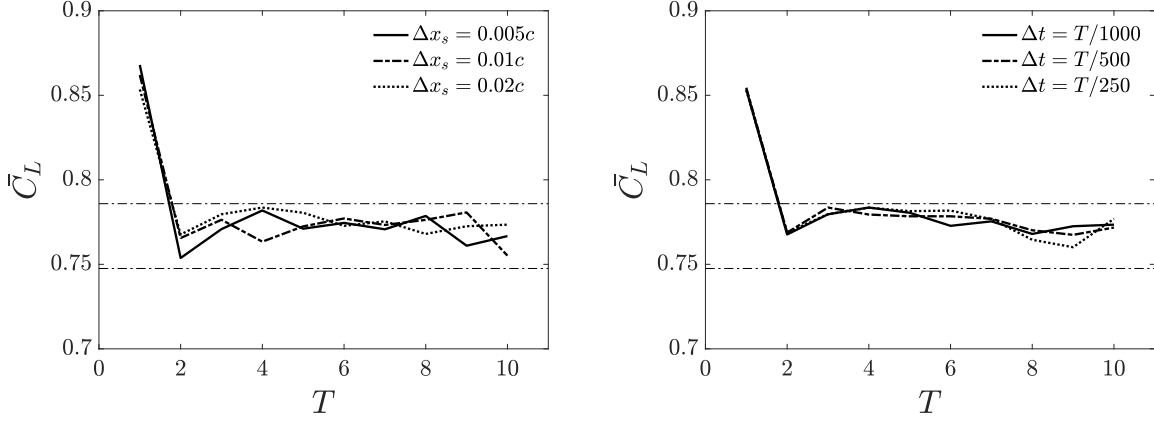
FIG. 3. Period-averaged lift coefficient $\bar{C}_L$ as a function of the flapping period T obtained with spatial resolutions $\Delta x_s = 0.005c$, $0.01c$ and $0.02c$ (left, $\Delta t = T/1000$) and temporal resolutions $\Delta t = T/1000$, $T/500$ and $T/250$ (right, $\Delta x_s = 0.02c$).

radial position $r = 0.716R$ during the constant revolving speed phase. Accordingly, the mean horizontal force is zero for all cases. C_P is derived from both revolving Q_R and pitching Q_P torques: $C_P = -2(\dot{\phi}Q_R + \dot{\alpha}Q_P)/\rho S U^3$, where $\dot{\phi}$ and $\dot{\alpha}$ are the revolving and pitching angular velocities. Note that instants with negative C_P correspond to phases where aerodynamic forces do not oppose the wing motion. By accounting for these negative contributions in the computation of the time-averaged power coefficient, it is assumed that power can be stored and recovered. Nevertheless, although not shown here for the sake of conciseness, we mention that present results do not significantly change whether we account for these negative contributions or not.

Labels in figure 4 indicate the (α_1, α_2) pair for each point and curves are used to connect points with similar α_1. Due to the hovering flight condition, the stroke plane is tilted clockwise with respect to that shown in figure 1 when $\alpha_1 \geq \alpha_2$, and hence α_1 corresponds to the downstroke angle of attack (i.e. the wing moves downward as it revolves from left to right). Conversely, the stroke plane is tilted anti-clockwise with respect to that shown in figure 1 when $\alpha_1 < \alpha_2$, and hence α_1 corresponds to the upstroke angle of attack (i.e. the wing moves upward as it revolves from left to right).

Figure 4 shows that for all α_1 curves (i.e. $\alpha_1 = 20°$, $30°$, $45°$ and $60°$), both $\bar{C}_V$ and $\bar{C}_V/\bar{C}_P$ increase with α_2 until a maximum $\bar{C}_V/\bar{C}_P$ on the order of 1.3 is reached. $\bar{C}_V/\bar{C}_P$ then drops with α_2 while C_V continues to increase until it peaks around values close to 0.8.
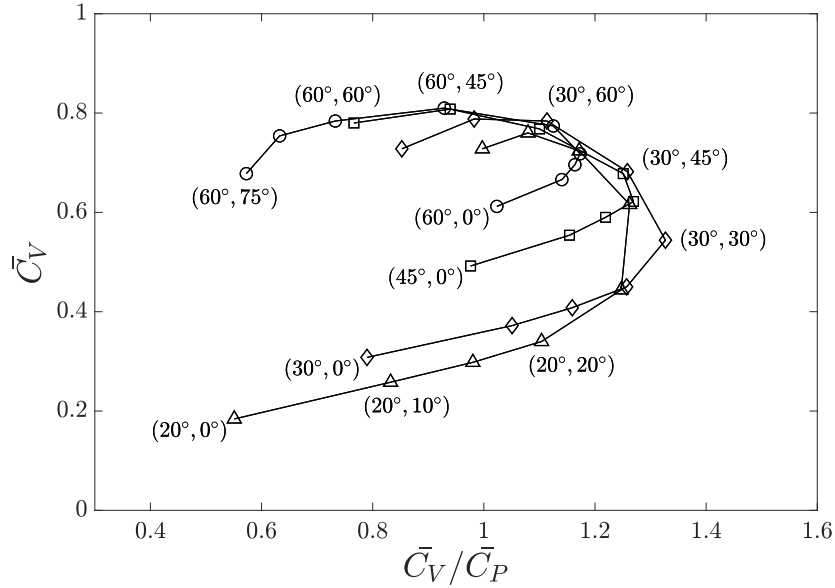
8

FIG. 4. Time-averaged vertical force coefficient $\bar{C}_V$ as a function of time-averaged vertical force coefficient to power coefficient ratio $\bar{C}_V/\bar{C}_P$ obtained for different (α_1, α_2) configurations.

It is striking that maximum values of C_V and C_V/C_P are of the same order of magnitude for all curves.

Furthermore, it can be observed that asymmetry has distinct effects on $\bar{C}_V$ and $\bar{C}_V/\bar{C}_P$ depending on α_1. Table I reports, for each α_1 curve, variations in $\bar{C}_V$ and $\bar{C}_V/\bar{C}_P$ obtained for optimal cases (i.e. maximum C_V and maximum C_V/C_P cases obtained for a given α_1) with respect to symmetric cases. The value of α_2 for which these optimal cases are reached is indicated in brackets. Overall, it appears that asymmetry offers the potential to increase both $\bar{C}_V$ and $\bar{C}_V/\bar{C}_P$ for all α_1. Yet, it is observed that the potential increase in $\bar{C}_V$ is larger for low values of α_1 while the potential increase in $\bar{C}_V/\bar{C}_P$ is larger for high values of α_1. At this point, present results thus support previous observations on two-dimensional configurations where asymmetry was found to promote aerodynamic performance[6–8]

In order to provide further insight into the cause for increases in $\bar{C}_V$ and $\bar{C}_V/\bar{C}_P$ with asymmetry we first display $\bar{C}_V$ and $\bar{C}_V/\bar{C}_P$ as a function of β in figure 5. β is an indirect measure of the degree of asymmetry (i.e. its magnitude increases with the difference between α_1 and α_2) and reflects the contribution of drag to the vertical force (i.e. drag contribution increases with β). Figure 5 shows that maxima in $\bar{C}_V$ and $\bar{C}_V/\bar{C}_P$ are obtained for very different values of β and hence that stroke plane inclination, and in turn the relative im-

9

α_1	max. $\bar{C}_V$ (α_2)	max. $\bar{C}_V/\bar{C}_P$ (α_2)
20°	+124% (75°)	+14% (45°)
30°	+45% (75°)	0% (30°)
45°	+5% (60°)	+15% (20°)
60°	+3% (45°)	+60% (20°)

TABLE I. Variations in $\bar{C}_V$ and $\bar{C}_V/\bar{C}_P$ obtained for optimal cases with respect to their symmetric counterparts. Reference values for $\bar{C}_V$ and $\bar{C}_V/\bar{C}_P$ are 0.34 and 1.10 for (20°,20°), 0.54 and 1.33 for (30°,30°), 0.77 and 1.10 for (45°,45°), 0.78 and 0.73 for (60°,60°).
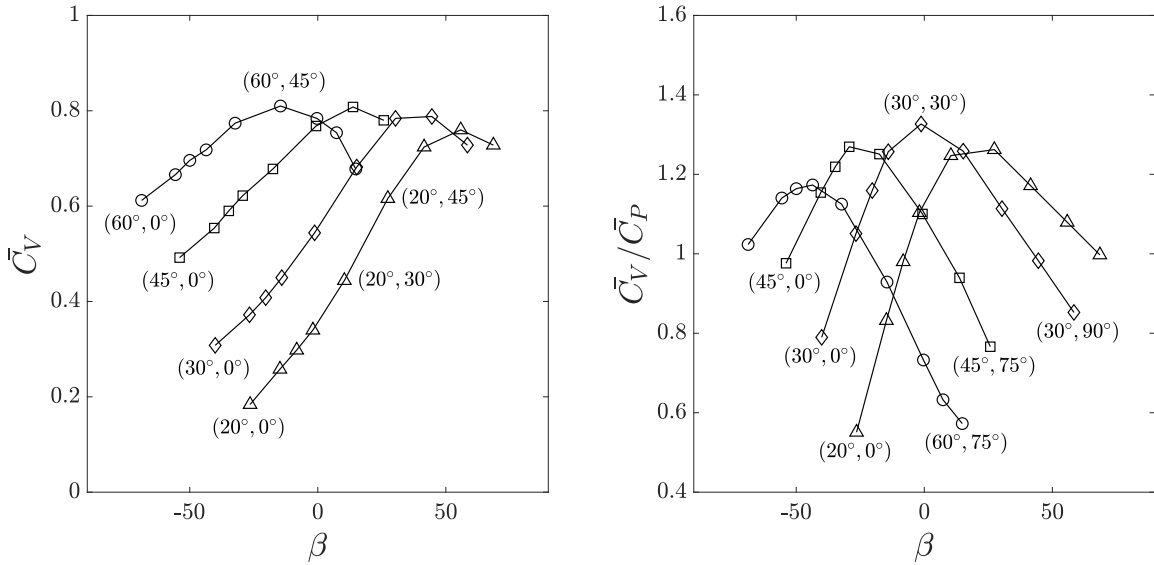

FIG. 5. $\bar{C}_V$ (left) and $\bar{C}_V/\bar{C}_P$ (right) as a function of stroke plane angle β obtained for different (α_1, α_2) configurations.

portance of drag contribution to the vertical force, is not what drives, to leading order, the observed enhancement in aerodynamic performance.

Alternatively, figure 6 plots $\bar{C}_V$ and $\bar{C}_V/\bar{C}_P$ as a function of the mean angle of attack $\bar{\alpha}$. It is shown that all α_1 curves nearly collapse onto a single curve, highlighting the prominent role of $\bar{\alpha}$ in the observed enhancement of aerodynamic performance. While a relatively clear collapse is observed for $\bar{C}_V$, some offsets exists for $\bar{C}_V/\bar{C}_P$ which indicates that additional parameters mitigate the effect of $\bar{\alpha}$. Yet, it is worth stressing that, within the range of cases tested, maximum efficiency is reached for the symmetric case $\alpha_1 = \alpha_2 = 30°$. In
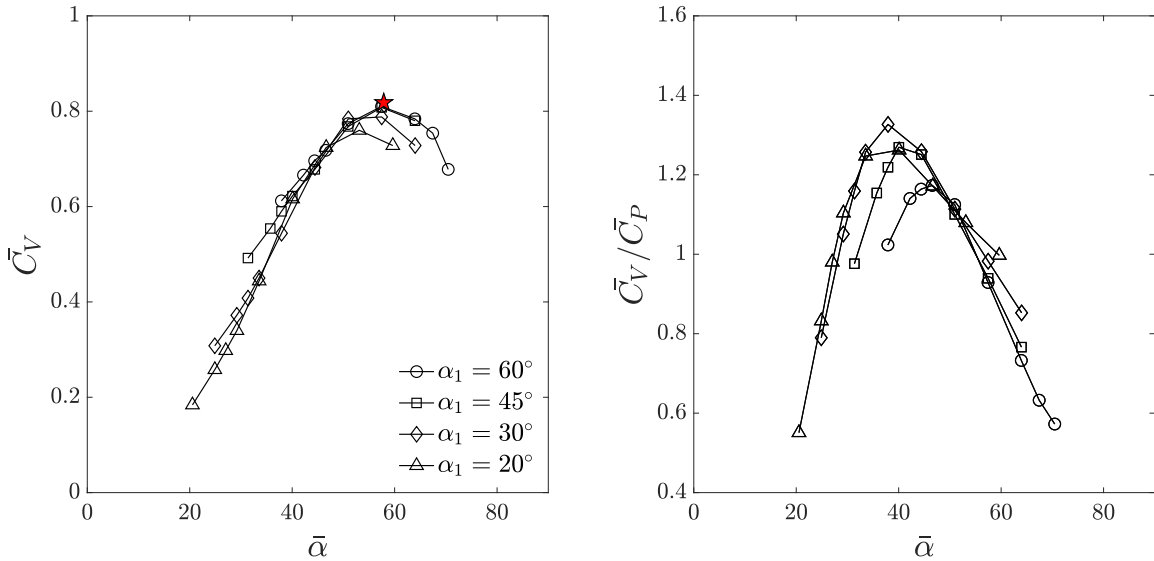
FIG. 6. $\bar{C}_V$ and $\bar{C}_V/\bar{C}_P$ as a function of mean angle of attack $\bar{\alpha}$ obtained for different (α_1, α_2) configurations.

addition, the symmetric case $\alpha_1 = \alpha_2 = 53°$ (which yields $\bar{\alpha} = 57°$ for which $\bar{C}_V$ is found to be maximum) has been simulated, leading to the optimal $\bar{C}_V$ value depicted with a red star on figure 6. Therefore, these results suggest that, to leading order, asymmetry is not responsible for neither the maximum in $\bar{C}_V$ nor that in $\bar{C}_V/\bar{C}_P$.

B.   Unsteady aerodynamics

We now use higher fidelity numerical simulations ($\Delta x_s = 0.01c$ and $\Delta t = T/1000$) to analyze the unsteady aerodynamics of specific cases that exhibit good aerodynamic performance, i.e. cases that rely on or close to the Pareto front in figure 4.

Figure 7 displays a time sequence of non-dimensional Q criterion isosurfaces for a reference symmetric case (45°, 45°) after 10 flapping cycles. At $t/T = 0$ (figure 7(a)), the wing initiates the downstroke phase and is about to revolve from left to right. The flow is characterized by a conical LEV that extends from the wing root to the tip. As will be discussed, the LEV bursts near the wing tip as it merges with the tip vortex (TV) which hence exhibits a relatively complex structure in the wake of the wing. A trailing edge vortex induced by the pitching motion of the wing, sometimes referred to as rotational vortex (RV), is also visible in the vicinity of the trailing edge. As the wing starts to revolve, it interacts with the LEV-
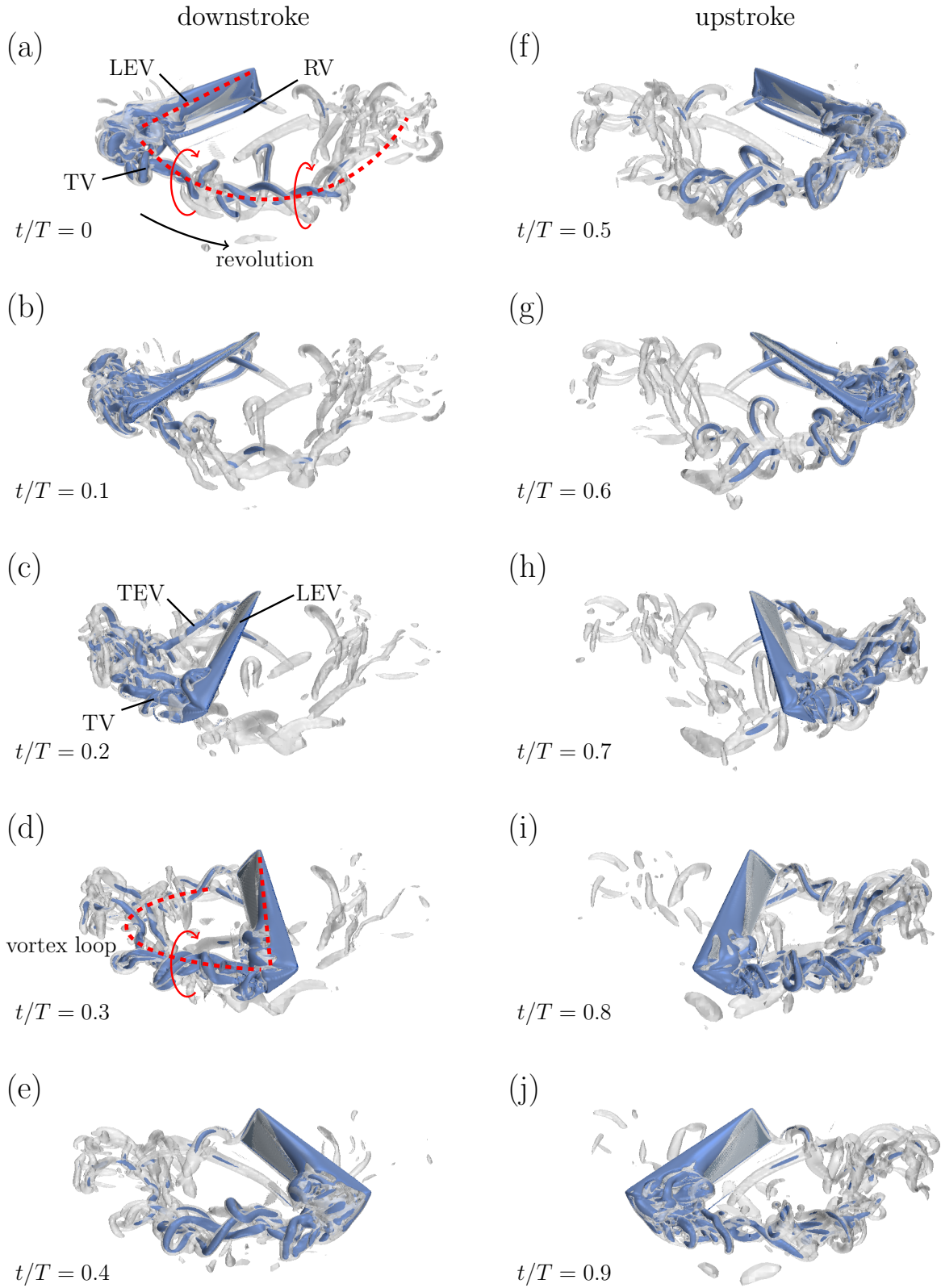
11

FIG. 7. Q-criterion isosurfaces obtained at different instants t/T (a-j) for the reference (45°, 45°) case.

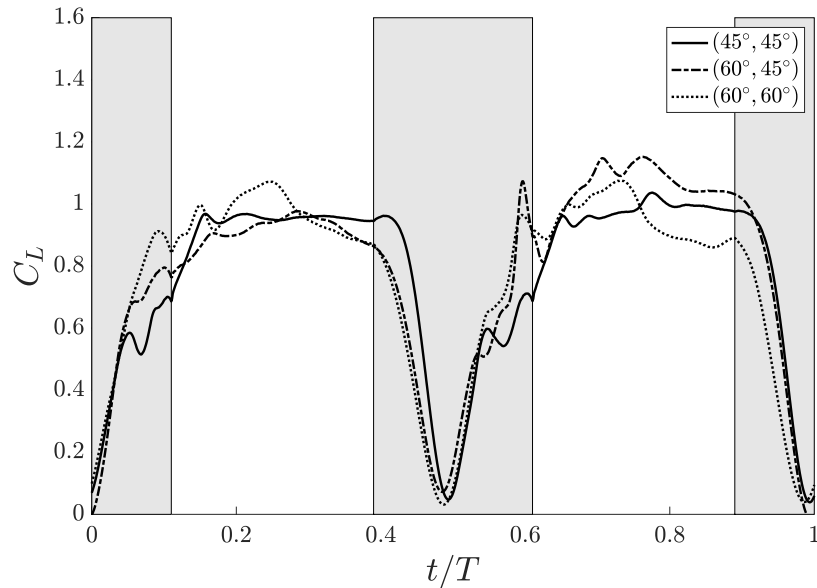FIG. 8. Instantaneous lift coefficient C_L as a function of non-dimensional time t/T obtained for cases (45°, 45°), (60°, 45°) and (60°, 60°).

TV structure and a new LEV forms on the opposite surface of the wing (figure 7(b,c)). This new LEV is similar to that of the previous stroke, exhibiting a conical shape that rapidly bursts into smaller scale structures as it merges with the new TV. A trailing edge vortex (TEV) also forms that connects with the new LEV-TV structure, forming a LEV-TV-TEV vortex loop (figure 7(d)). The sense of rotation of this vortex loop is such that momentum is carried downwards within the area swept by the wing, reflecting the production of lift. The resulting downwash tends to reduce the effective angle of attack of the wing which explains why maximum vertical force was obtained for mean angles of attack as large as $\bar{\alpha} = 57°$ in figure 6. The radial position where the LEV bursts is around $0.7R$ at $t/T = 0.25$ but rapidly moves inboard as the wing undergoes both pitching and decelerating motions at the end of the downstroke phase (figure 7(e,f)). Vortex burst has been shown to result from the competition between outboard flow inside the LEV due to spanwise gradients in flow speed and rotational accelerations and inboard flow due to the TV (e.g.[22]). Deceleration presumably induces a reduction in outboard flow which results in the inboard displacement of the equilibrium position between outbard and inboard flow. The motion being symmetric the flow during the following upstroke phase is qualitatively similar to that observed during the downstroke phase (figure 7(g-j)).

The corresponding instantaneous lift coefficient C_L is displayed in figure 8 as a function of the non-dimensional time t/T, along with those obtained for cases (45°, 60°) and (60°, 60°). Grayed regions indicate pronation and supination phases where the wing is undergoing both pitching motion and revolving acceleration/deceleration (i.e. over t_p). Conversely, white regions indicate phases where the wing has constant angle of attack and constant revolving speed.

The symmetric, reference case (45°, 45°) demonstrates similar lift production during downstroke and upstroke phases, with C_L plateauing around 0.95 during the constant revolving speed phases. Moreover, it can be observed that during the acceleration phase, the increase in C_L is not as smooth as one would expect from the contribution of quasi-steady, rotational (sometimes referred to as the Kramer effect) and added mass effects. This suggests that non-linear wake capture effects tend to mitigate lift production. This appears to be rather different for the two other cases (60°, 45°) and (60°, 60°) where C_L does not exhibit clear troughs during the beginning of the downstroke phase and exhibit relatively large peaks at the beginning of the upstroke phase, around $t/T \approx 0.6$. Interestingly, a consequence of this different dynamics is that cases (45°, 45°) and (60°, 45°) achieve different levels of lift during the constant revolving speed phase of the upstroke, although the upstroke angle of attack is the same. Specifically, the time-averaged lift coefficient over this constant speed phase is about 10% larger for the (60°, 45°) case than for the (45°, 45°) case.

In order to clarify these differences, figure 9 displays time sequences of non-dimensional spanwise vorticity obtained for cases (45°, 45°), (60°, 45°) and (60°, 60°) at radial station $0.716R$ (i.e. the reference spanwise cross-section) at the beginning of the downstroke phase. For comparison purposes, snapshots are oriented in such a way that the wing path is horizontal, which is the case for symmetric cases (or nearly horizontal due to chaotic fluctuations from one stroke to another, i.e. $\beta \approx 0°$) but not for asymmetric cases, see figure 5. At $t/T = 0.02$ the flow is characterized by the LEV that developed during the previous upstroke and the RV induced by the pitching motion, as previously discussed from figure 7. In the (45°, 45°) case, the wing interacts with the LEV in such a way that it 'slips' on the lower surface ($t/T = 0.04$ and $t/T = 0.06$) and ultimately feeds with vorticity the TEV that concomittantly forms as the wing revolves from left to right ($t/T = 0.08$). Because the LEV acts as a low pressure region, it has a negative contribution to lift, which explains the mitigated increase in C_L discussed earlier. On the contrary, the LEV interacts with the
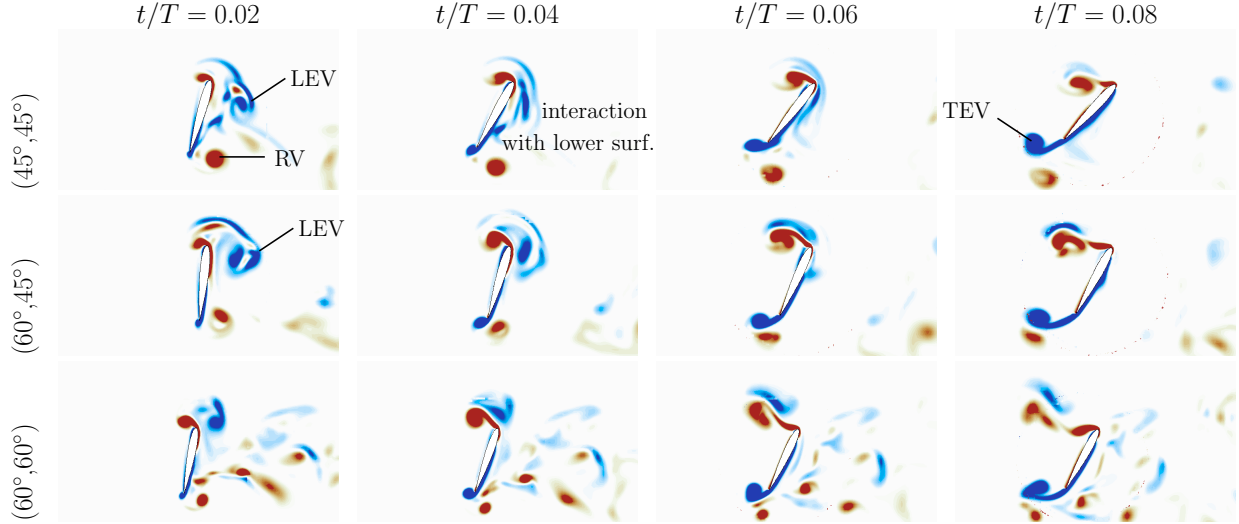
14

FIG. 9. Spanwise vorticity contours obtained in the $r = 0.716R$ spanwise cross-section at different instants t/T during early downstroke for cases $(45°, 45°)$, $(60°, 45°)$ and $(60°, 60°)$.
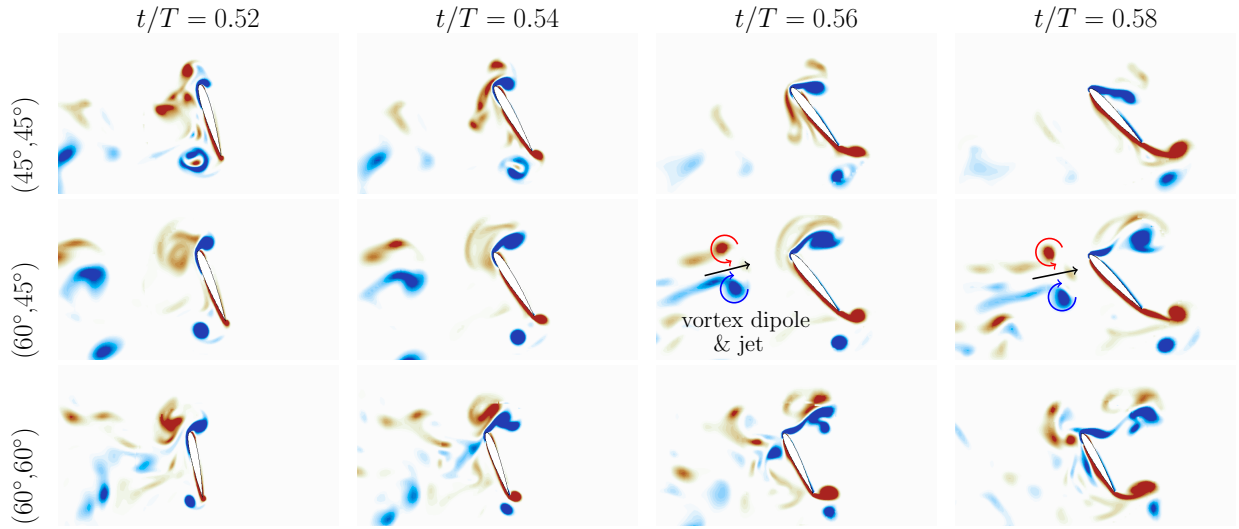

FIG. 10. Spanwise vorticity contours obtained in the $r = 0.716R$ spanwise cross-section at different instants t/T during early upstroke for cases $(45°, 45°)$, $(60°, 45°)$ and $(60°, 60°)$.

leading edge and most of the vorticity passes above the wing in case $(60°, 45°)$. This trend is even more pronounced in case $(60°, 60°)$ where the LEV appears to remain above the wing for the full sequence and, accordingly, where the resulting lift coefficient exhibits a rather smooth increase.

Figure 10 displays similar time sequences for the beginning of the upstroke phase. The flow fields in the $(45°, 45°)$ case are qualitatively similar to those observed during the down-
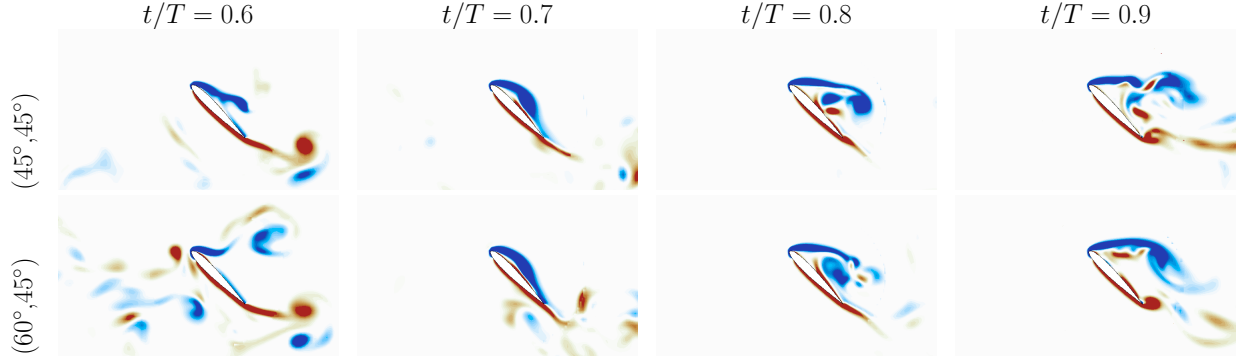
FIG. 11. Spanwise vorticity contours obtained in the $r = 0.716R$ spanwise cross-section at different instants t/T during upstroke for cases (45°, 45°) and (60°, 45°).

stroke owing to the symmetry of the kinematics. Conversely, while the (60°, 60°) case is also symmetric, slight differences exist in the wake structure which result in non-negligible differences in lift production between early downstroke and early upstroke phases. For example, the flow at $t/T = 0.56$ and $t/T = 0.58$ exhibits secondary vortical structures that interact with the wing, a feature that is not clearly observed during early downstroke and that may be responsible for the non-linear increase in C_L. We note that slight differences between upstroke and downstroke may arise despite symmetrical kinematics due to the chaotic nature of the flow which is here emphasized by the occurence of LEV burst. On the other hand, the flow fields in the (60°, 45°) case significantly differ from those observed during the downstroke phase. In particular, a relatively strong vortex dipole generated during downstroke is observed, with a resulting fluid velocity directed towards the lower surface of the wing. This structure affects both effective angle of attack and relative flow velocity, which results in the lift peak observed near $t/T = 0.6$ on figure 8. Wake capture mechanisms are further assessed in appendix B.

A consequence of these significantly different wake capture mechanisms between cases (45°, 45°) and (60°, 45°) is the difference in LEV dynamics during the constant revolving speed phase of the upstroke, although the two cases have similar kinematics, i.e. with similar upstroke angle of attack. Figure 11 shows time sequences of non-dimensional spanwise vorticity obtained for cases (45°, 45°) and (60°, 45°) at radial station $0.716R$ and times $t/T \in [0.6; 0.9]$. It can be observed that at $t/T = 0.7$, the LEV develops slightly closer to the airfoil surface in the (60°, 45°) case and that at $t/T = 0.8$, it is still predominantly upstream of the trailing edge (as opposed to case (45°, 45°)), which are two features that
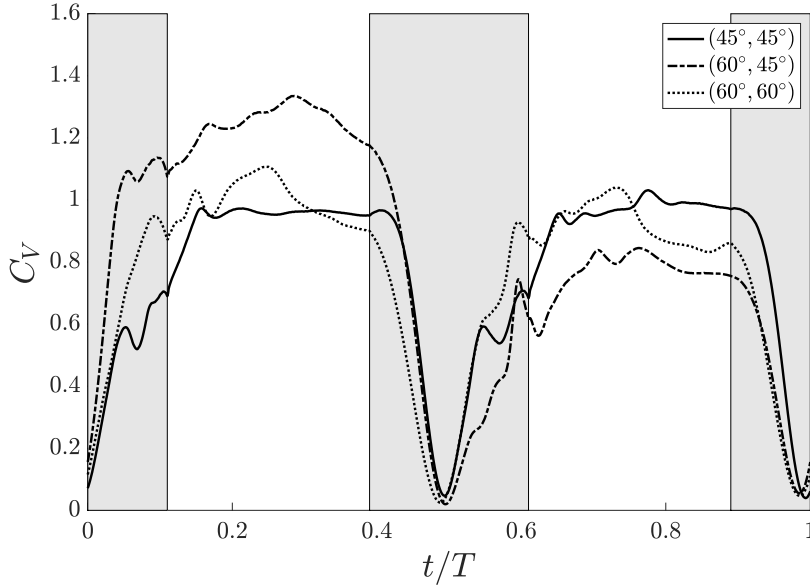
FIG. 12. Instantaneous vertical force coefficient C_V as a function of non-dimensional time t/T obtained for cases $(45°, 45°)$, $(60°, 45°)$ and $(60°, 60°)$.

promote lift generation[23]. These differences are believed to be responsible for differences in lift production during the constant revolving speed phase.

The instantaneous vertical force component resulting from the contributions of both lift and drag is shown in figure 12 for the three cases $(45°, 45°)$, $(60°, 45°)$ and $(60°, 60°)$. Note that the net force generated in such massively separated flows has been shown to act normally to the wing surface (e.g.[24]) and hence the drag exhibits a similar trend to that observed for lift. This point is further discussed in appendix C. Figure 12 shows that C_V is significantly larger for case $(60°, 45°)$ during the downstroke due to drag contribution (as opposed to other symmetric cases where C_V only results from lift contribution). Specifically, the downstroke time-averaged vertical force obtained for $(60°, 45°)$ is 34% and 33% larger than that obtained for $(45°, 45°)$ and $(60°, 60°)$ respectively. This gain in C_V is partly counterbalanced by the negative contribution of drag to C_V during upstroke, with upstroke time-averaged vertical force obtained for $(60°, 45°)$ 23% and 19% lower than that obtained for $(45°, 45°)$ and $(60°, 60°)$ respectively. Yet, this negative contribution does not fully compensate for the positive contribution during downstroke. While this may partly result from differences in wake capture and subsequent LEV dynamics highlighted previously, the overall gain in $\bar{C}_V$ obtained for $(60°, 45°)$ with respect to $(45°, 45°)$ and $(60°, 60°)$ cases is
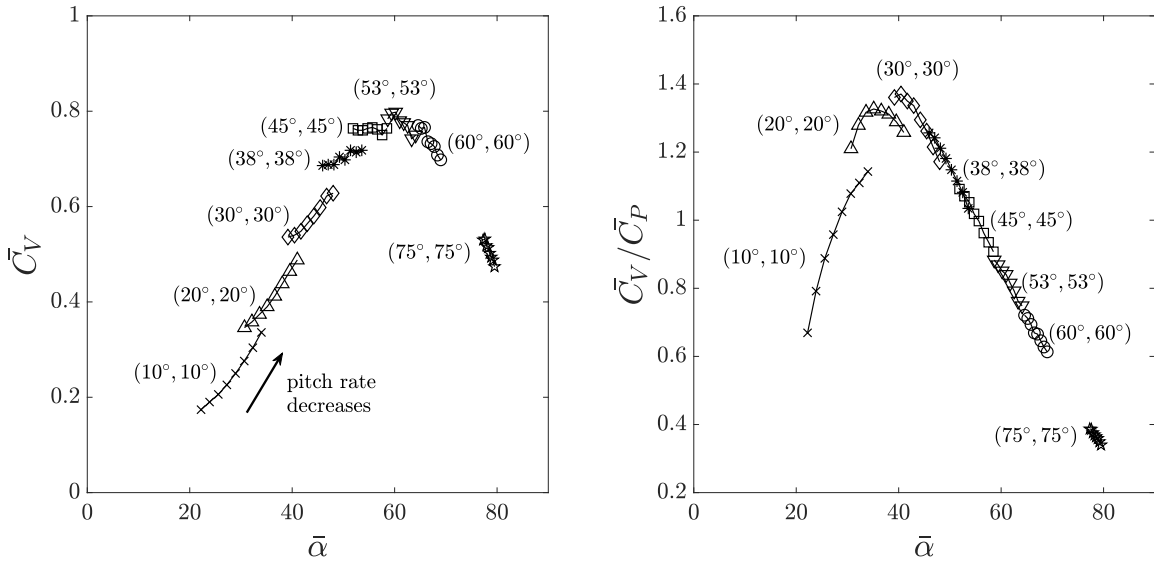
17

FIG. 13. $\bar{C}_V$ (left) and $\bar{C}_V/\bar{C}_P$ (right) as a function of mean angle of attack $\bar{\alpha}$ obtained for symmetric cases ($\alpha_1 = \alpha_2$) with different pitch rates.

primarily due to $\bar{\alpha}$ being closer to the optimal value ($\bar{\alpha} \approx 51°$, $57°$ and $64°$ for cases ($45°$, $45°$), ($60°$, $45°$) and ($60°$, $60°$) respectively, see figure 6). In other words, wake capture is, within the range of cases tested, not what drives aerodynamic performance in the time-averaged sense, to leading order. However, it may contribute to generating large transient loads and hence play a role in enhanced maneuverability, providing that it occurs on a sufficiently large time scale to affect the motion of the whole body.

C.   Extension to various pitch rates

In order to further assess the role of $\bar{\alpha}$ on aerodynamic performance, we perform additional simulations varying the pitch rate. A decrease in pitch rate leads to an increase in $\bar{\alpha}$ but may here again significantly affect wake capture mechanisms. In addition, it directly influences transient loads through changes in rotational circulation (Kramer effect) and added mass effects.

Figure 13 depicts $\bar{C}_V$ and $\bar{C}_V/\bar{C}_P$ as a function of $\bar{\alpha}$ for various symmetric cases with different pitch rates. Recall that the pitch rate is here parameterized by the time t_p over which the pitching motion occurs, which is here varied from 11% to 25% of the flapping period T (cases in previous sections had t_p set to 11% of the flapping period). Data points
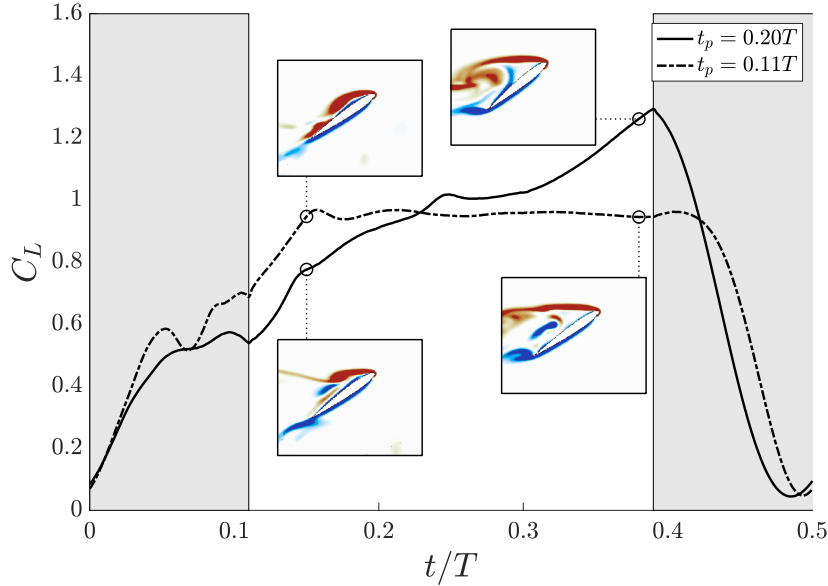
18

FIG. 14. Instantaneous lift coefficient C_L as a function of non-dimensional time t/T obtained for cases (45°, 45°) with different pitch rates. Insets display spanwise vorticity contours obtained in the $r = 0.716R$ spanwise cross-section at two instants.

are found to cluster on similar curves to those identified for asymmetric cases in figure 6, with a maximum $\bar{C}_V$ of approximately 0.8 reached near $\bar{\alpha} = 57°$ and a maximum $\bar{C}_V/\bar{C}_P$ of approximately 1.4 near $\bar{\alpha} = 38°$. The continuity in $\bar{C}_V/\bar{C}_P$ between configurations with different (α_1, α_2) settings for $\bar{\alpha} > 38°$ is particularly striking.

Figure 14 displays the time history of C_L obtained for (45°, 45°) and pitch durations corresponding to 11% and 20% of the flapping period T. Again, we show that instantaneous lift coefficients can exhibit significantly different trends at the beginning and end of the strokes due to differences in angle-of-attack, added mass effects, rotational effects and wake capture mechanisms, but still yield similar time-averaged lift, which supports previous observations on asymmetric cases. In particular, insets in figure 14 highlight different LEV dynamics with larger instantaneous lift associated with the LEV being closer to the wing surface.

IV. CONCLUSION

While most insects rely on 'normal' hovering flapping flight, some of the best hoverers flap their wings along an inclined stroke plane. Most probably because of their underrepresenta-

tion in nature, the latter has been relatively unexplored as compared to 'normal' hoverers, although it has been suggested that they may exhibit enhanced aerodynamic performance due to the contribution of drag to the vertical force (i.e. and not only to that opposing the wing motion).

In this paper, we have performed numerical simulations to assess the aerodynamic performance of various asymmetric flapping wing kinematics for which the hovering condition yields an inclined stroke plane. Simulations with relatively low spatial and temporal resolutions were first conducted to explore a rather large parameter space at reduced computational cost and unravel the key parameters that drive lift and lift-to-power ratio. Simulations with higher spatial and temporal resolutions were then conducted for cases located on the lift versus lift-to-power ratio Pareto front to evaluate unsteady mechanisms at play and further demonstrate the relevancy in using simulations with lower resolutions for parameter space exploration.

Overall, it was shown that lift and lift-to-power ratio of various asymmetric kinematics roughly collapse onto a single curve when plotted as a function of the mean angle of attack. Conversely, cases with similar stroke plane inclination may lead to very distinct lift and lift-to-power ratios which indicates that stroke plane inclination, hence the relative contribution of drag to vertical force, is not what drives aerodynamic performance in 'non-normal' hovering flapping flight. In addition, the analysis of unsteady aerodynamic forces and associated flow physics revealed that, within the range of cases tested here, wake capture mechanisms, added mass and rotational (Kramer) effects only marginally affect time-averaged aerodynamic performance which is driven by the mean angle of attack, to leading order. This was further supported by additional symmetric cases with various pitch rates. Yet, we stress that different kinematics with similar mean angle of attack may lead to different instantaneous forces due to different wake capture mechanisms, added mass and rotational (Kramer) effects and that large aerodynamic forces may contribute to enhanced maneuverability providing that they occur on a sufficiently large time scale to affect the motion of the whole body.

These results shed a new light on previous hypothesis on potentially enhanced performance of asymmetric hovering flapping flight. Yet, while a relatively large number of configurations was tested, the parameter space that characterizes hovering flapping wings is vast and future work is needed to evaluate to what extent do present results hold for other kinematics and wing geometries.
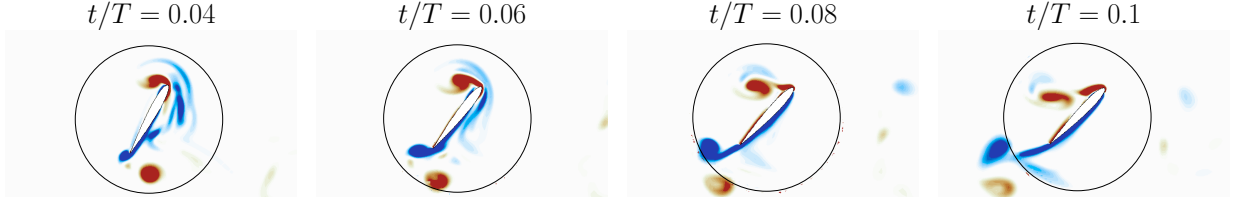
FIG. 15. Spanwise vorticity contours obtained in the $r = 0.716R$ spanwise cross-section at different instants t/T during downstroke for case (45°, 45°). The black line shows the position of the interpolation region between inner moving and background fixed meshes.

APPENDIX A : OVERSET MESH

The inner cylindrical domain enclosing the wing is designed such that most of the vorticity remains inside of it, which is here made possible by the fact that the LEV remains attached to the wing along most of the wing span and the flapping cycle. As such, interpolations between the inner moving domain and the outer fixed domain have a limited impact on the flow dynamics. Yet, some structures do pass through the interpolation region that connects the solutions of the inner and outer meshes. This is shown in figure 15 which depicts vorticity contours obtained in the $r = 0.716R$ section at different instants for the reference symmetric case shown in figure 1. The black line marks the position of the interpolation region. It can be observed that the vortex dipole that passes through this line, in the vicinity of the trailing edge, does not suffer from significant numerical dissipation due to the interpolation scheme. We note that the latter relies on a distance weighted approach with a typical ratio between inner and outer cell sizes equal to two.

APPENDIX B : WAKE CAPTURE MECHANISMS

Wake capture mechanisms can further be assessed by comparing the time history of C_L obtained after 10 flapping cycles with that obtained at the very first stroke (which is free of any wing-wake interactions), as depicted in figure 16 for the (45°, 45°) case. The difference between the two strokes results from interactions with vortical structures and general downwash from previous strokes. It is clearly shown that wake capture mechanisms at the beginning of the 21st stroke have a strong, negative impact on lift production. It is also clear that the general downwash, together with wing-wake interactions effect on LEV
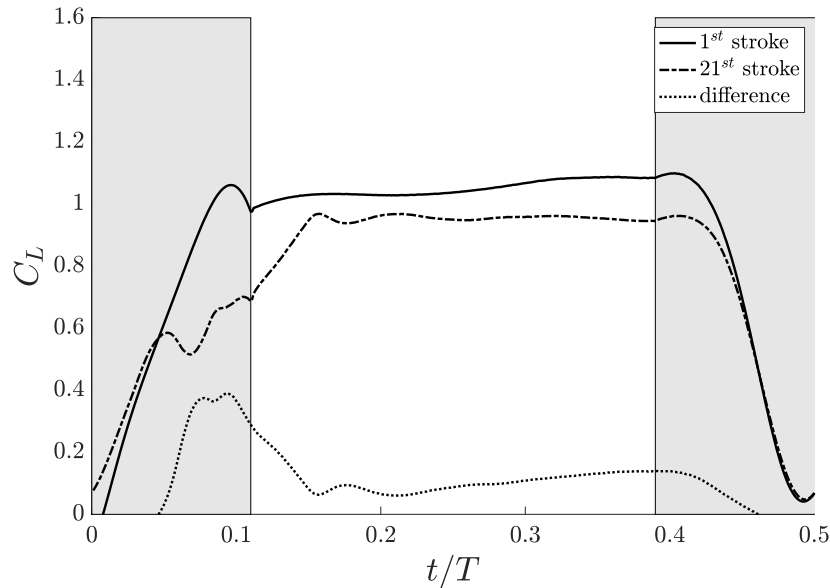
21

FIG. 16. Instantaneous lift coefficient C_L as a function of non-dimensional time t/T obtained during the 1st and 21st strokes of case (45°, 45°) and corresponding difference.

formation, tends to reduce lift during the constant revolving speed phase, to a lesser extent though.

APPENDIX C : NORMAL FORCE AND STROKE PLANE INCLINATION

Massively separated flows induce a pressure force that acts normally to the wing surface. A direct consequence is that, in order for the wing to generate a pure vertical force (i.e. no horizontal force), the wing chord should be oriented along the horizontal axis. That is, if one considers a single stroke with angle of attack α_1, then the stroke plane should be tilted with an angle $\beta_1 = -\alpha_1$. This is similar for the returning stroke with angle of attack α_2 where the stroke plane should be tilted with an angle $\beta_2 = \alpha_2$. The overall stroke plane angle is then $\beta = \beta_1 + \beta_2 = \alpha_2 - \alpha_1$. This relation is depicted on figure 17 and is found to provide a good approximation of data obtained from present numerical simulations.
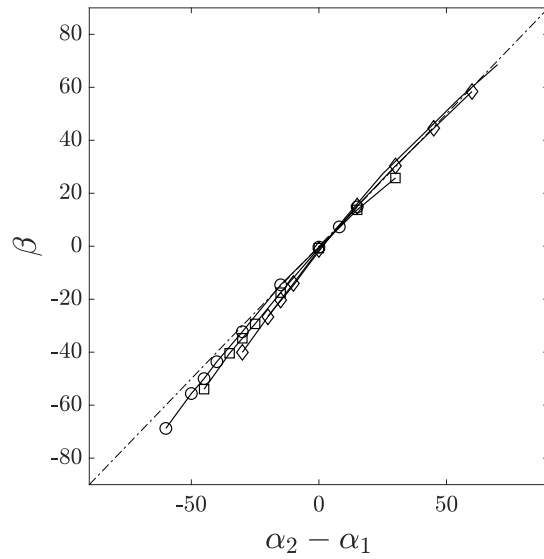
22

FIG. 17. Stroke plane angle β as a function of the difference between angles of attack of two consecutive strokes $\alpha_2 - \alpha_1$ obtained for different (α_1, α_2) configurations. The dashed line depicts the $\beta = \alpha_2 - \alpha_1$ relation.

ACKNOWLEDGEMENTS

AUTHOR DECLARATION

The authors declare that they have no conflict of interest.

DATA AVAILABILITY

The data that support the findings of this study are available from the corresponding author upon reasonable request.

REFERENCES

[1] T. Weis-Fogh, "Quick estimates of flight fitness in hovering animals, including novel mechanisms for lift production," J. Exp. Biol. **59**, 169–230 (1973).

[2] B. W. Tobalske, D. R. Warrick, C. Clark, D. Powers, T. Hedrick, G. Hyder, and A. A. Biewener, "Three-dimensional kinematics of hummingbird flight," J. Exp. Biol. **210**, 2368–2382 (2007).

[3] W. Shyy, H. Aono, S. Chimakurthi, P. Trizila, C. Kang, C. Cesnik, and H. Liu, "Flight force production by flapping insect wings in inclined stroke plane kinematics," Prog. Aerosp. Sci. **46**, 284–327 (2010).

[4] M. Thakor, G. Kumar, D. Das, and A. De, "Investigation of asymmetrically pitching airfoil at high reduced frequency," Phys. Fluids **32**, 053607 (2020).

[5] C. Hefler, R. Noda, H. Qiu, and W. Shyy, "Aerodynamic performance of a free-flying dragonfly—a span-resolved investigation," Phys. Fluids **32**, 041903 (2020).

[6] Z. Wang, "The role of drag in insect hovering," J. Exp. Biol. **207**, 4147–4155 (2004).

[7] Y. Sudhakar and S. Vengadesan, "Flight force production by flapping insect wings in inclined stroke plane kinematics," Comput. Fluids **39**, 683–695 (2010).

[8] T. Jardin, L. David, and A. Farcy, "Characterization of vortical structures and loads based on time-resolved PIV for asymmetric hovering flapping flight," Exp. Fluids **46**, 847–857 (2009).

[9] C. Wang, C. Zhou, and P. Xie, "Numerical investigation on aerodynamic performance of a 2-d inclined hovering wing in asymmetric strokes," J. Mech. Sci. Technol. **30**, 199–210 (2016).

[10] D. Lentink and M. Dickinson, "Rotational accelerations stabilize leading edge vortices on revolving fly wings," J. Exp. Biol. **212**, 2705–2719 (2009).

[11] T. Jardin, "Coriolis effect and the attachment of the leading edge vortex," J. Fluid Mech. **820**, 312–340 (2017).

[12] N. Werner, H. Chung, J. Wang, G. Liu, J. Cimbala, H. Dong, and B. Cheng, "Radial planetary vorticity tilting in the leading-edge vortex of revolving wings," Phys. Fluids **31**, 041902 (2019).

[13] H. Park and H. Choi, "Kinematic control of aerodynamic forces on an inclined flapping wing with asymmetric strokes," Bioinspir. Biomim. **7**, 016008 (2012).

[14]H. Zhu and M. Sun, "Unsteady aerodynamic force mechanisms of a hoverfly hovering with a short stroke-amplitude," Phys. Fluids **29**, 081901 (2017).

[15]J. Zhang and W. Huang, "On the role of vortical structures in aerodynamic performance of a hovering mosquito," Phys. Fluids **31**, 051906 (2019).

[16]T. Jardin and T. Colonius, "On the lift-optimal aspect ratio of a revolving wing at low reynolds number," J. Roy. Soc. Interface **15**, 20170933 (2018).

[17]S. Muzaferija, *Adaptive finite volume method for flow prediction using unstructured meshes and multigrid approach*, Ph.D. thesis, Univ. London (1994).

[18]I. Demirdžić and S. Muzaferija, "Numerical method for coupled fluid flow, heat transfer and stress analysis using unstructured moving meshes with cells of arbitrary topology," Comput. Meth. Appl. Mech. Engng **125**, 235–255 (1995).

[19]Y. Bury and T. Jardin, "Transitions to chaos in the wake of an axisymmetric bluff body," Phys. Lett. A **376**, 3219–3222 (2012).

[20]T. Jardin and L. David, "Root cutout effects on the aerodynamics of a low-aspect-ratio revolving wing," AIAA J. **55**, 2717–2726 (2017).

[21]T. Jardin and N. Doué, "Influence of pitch rate on freely translating perching airfoils," J. Fluid Mech. **873**, 49–71 (2019).

[22]A. Medina and A. Jones, "Leading-edge vortex burst on a low-aspect-ratio rotating flat plate," Phys. Rev. Fluids **1**, 044501 (2016).

[23]T. Jardin, J. Choi, and T. Colonius, "An empirical correlation between lift and the properties of leading edge vortices," Theor. Comp. Fluid Dyn. (accepted).

[24]C. Pitt-Ford and H. Babinsky, "Lift and the leading-edge vortex," J. Fluid Mech. **720**, 280–313 (2013).